Journal of Magnetism and Magnetic Materials 493 (2020) 165692

Contents lists available at ScienceDirect

Journal of Magnetism and Magnetic Materials

journal homepage: www.elsevier.com/locate/jmmm

Research articles

Magnetic and magneto-optical properties of Fe_3O_4 nanoparticles modified with Ag

D.A. Petrov[a,*], R.D. Ivantsov[a], S.M. Zharkov[a,b], D.A. Velikanov[a,b], M.S. Molokeev[a,b], C.-R. Lin[c,*], C.-T. Tso[c], H.-S. Hsu[c], Y.-T. Tseng[c], E.-S. Lin[c], I.S. Edelman[a]

[a] Kirensky Institute of Physics SB RAS, Krasnoyarsk 660036, Russia
[b] Siberian Federal University, Svobodny Av., 79, Krasnoyarsk 660041, Russia
[c] National Pingtung University, Pingtung City, Pingtung County 90003, Taiwan

ARTICLE INFO

Keywords:
Fe_3O_4–Ag nanostructures
Superparamagnetism
Magnetic circular dichroism

ABSTRACT

Effect of Ag inclusions on magnetic properties and magnetic circular dichroism (MCD) of Fe_3O_4 nanoparticles (NPs) in the mixed system of Fe_3O_4 and Ag NPs in dependence on the relative concentration of the components is presented. The samples were synthesized by the thermal decomposition of the mixture of constant concentration of $Fe(NO_3)_3{\cdot}9H_2O$ and varied concentration of $AgNO_3$. The synthesized powdered samples consisted of Fe_3O_4 and Ag NPs located very close with each other, and in the most cases the Fe_3O_4 NPs were bordered with the Ag nanocrystals. The Ag introducing in the samples does not effect, practically, in the Fe_3O_4 NPs morphology and size distribution. At the same time, Ag NPs in the powdered samples cause a decrease in the Fe_3O_4 NPs magnetization and shift of the blocking temperature to lower temperatures, both approximately proportional to the Ag concentration. Most significant changes are revealed in the MCD spectra in the energy region of 1.2–2.2 eV. We have discussed the influence of the Ag NPs on the MCD spectra features in terms of the charge-transfer electron transitions.

1. Introduction

Magnetite (Fe_3O_4) is known to mankind since ancient times. Nevertheless, it remains one of the most widely studied magnetic ordered compounds due to its extraordinary properties and diverse applications. Magnetite has the inverse spinel structure of the space group Fd3m. The oxygen ions, O^{2-}, form a face-centered-cubic (*fcc*) lattice. The unite cell contains eight Fe^{3+} and eight Fe^{2+} cations occupying octahedral positions (B positions), and eight Fe^{3+} cations in tetrahedral positions (A positions). Thus, the cations in the B and A positions form two magnetic sublattices with the oppositely directed magnetic moments and the total magnetic moment is determined by the B sublattice [1]. The electrons can hop between Fe^{2+} and Fe^{3+} ions at room temperature, what allows referring magnetite to an important class of half-metallic materials [2]. Development of the magnetic nanoparticles (NPs) synthesis technology has broadened the scope of the Fe_3O_4 application in optoelectronics [3], magnetic storage [4], and bio-inspired applications [5] because of Fe_3O_4 NPs excellent chemical stability and the ability to change essentially properties in dependence on the features of technological conditions. The particular attention is being paid now to an effect of noble metals as Ag and Au in the Fe_3O_4 NPs properties. Enhanced magnetic moment and strong catalytic and antibacterial activities of the Ag/Fe_3O_4 nanocomposites demonstrated their importance for potential application in water treatment and biomedical applications [6–10]. Nanoparticles Fe_3O_4–Ag are used to detect various poisonous substances, such as cyanide [11], fungicide [12], pesticide [13], lead [14], mercury [15] and enzymeless hydrogen peroxide [16]. Heterodimer nanocomposite system of Fe_3O_4–Ag particles presents a novel class of materials for simultaneous two-photon fluorescence imaging and magnetic manipulation [17]. Self-assembled thin films of Fe_3O_4–Ag composite nanoparticles can be used for spintronic applications [18]. Based on the Fe_3O_4@Ag core–shell magnetic nanoparticles, a new substrate for in situ detection and identification of organic pollutants was developed [19]. The great variety of possible applications of the Fe_3O_4–Ag and Fe_3O_4@Ag nanoparticles stimulates the development of different modifications of the nanoparticles preparation technologies with an aim of the optimal selection of materials for specific applications. Whatever the applications of the discussed nanoparticles, their magnetic properties, depending on the features of the synthesis technology, should be studied first of all, since they provide the ability to control the functionality of particles using a magnetic field. The thermal decomposition of the metal salts assisted by different surfactants and

* Corresponding authors.
E-mail addresses: irbiz@iph.krasn.ru (D.A. Petrov), crlinspin@gmail.com (C.-R. Lin).

https://doi.org/10.1016/j.jmmm.2019.165692
Received 15 April 2019; Received in revised form 4 July 2019; Accepted 9 August 2019
Available online 21 August 2019
0304-8853/

organic solvents is one of the methods used for synthesis of the iron oxide nanoparticles (e.g., [20,21]). By controlling the conditions of synthesis it is possible to obtain various products from the same substance. The thermal decomposition method is characterized by a number of advantages, in comparison with other methods of manufacturing monodisperse nanoparticles: the process is non-toxic, inexpensive and it allows produce large amount of monodisperse nanocrystals in a single reaction without a further size-sorting process [22].

Here we present the results of the magnetic properties study of the Ag assisted Fe_3O_4 nanoparticles fabricated in the one pot with the thermal decomposition of the mixture of $Fe(NO_3)_3{\cdot}9H_2O$ and $AgNO_3$. The effect of a wide range Ag concentration variations on the magnetic properties of NPs synthesized in such a way is revealed. This effect is most clearly manifested in the study of the spectral dependences of the magnetic circular dichroism (MCD). MCD is one of the powerful methods giving an information on magnetic and electronic properties of a substance [23]. MCD signal is due to the same electron transitions that are responsible for the electronic absorption spectrum, but because of the different selection rules [24] MCD spectrum is characterized by much narrower and better resolved lines comparing to the absorption spectrum. Several works are available in literature on the MCD spectral dependences of the Fe_3O_4 nanoparticles fabricated with different techniques [25–27] and Fe_3O_4 thin films [28,29]. As concerns nanocomposites containing Fe_3O_4 and Ag, we managed to find only a couple of papers in the current literature devoted to Faraday rotation (FR) in the Fe_3O_4/Ag containing ferrofluids [30] and the Fe_3O_4/Ag nanoparticles [31] fabricated in TeO_3-PbO-B_2O_3 glasses using the Fe and Ag magnetron RF sputtering with the subsequent glass thermal treatment. The FR value dependences on magnetic field was presented in [30] and the Verdet constant in dependence on the glass heat treatment temperature was presented in [31] for the He-Ne laser wave length (633 nm) in both cases. So to our best knowledge, magneto-optical spectra of Fe_3O_4/Ag nanocomposites are obtained here for the first time. Analysis of the MCD spectral information obtained in combination with the structural, morphological, and static magnetic data gave the possibility to understand deeper the Ag effect in the Fe_3O_4 nanoparticle properties.

2. Experimental

2.1. Synthesis procedure

To synthesize samples, the basic raw materials $Fe(NO_3)_3{\cdot}9H_2O$ and $AgNO_3$ in different concentrations were used. The atomic molar ratios of Ag/Fe in samples and weight ratios of $AgNO_3$/$Fe(NO_3)_3{\cdot}9H_2O$ in solutions are presented in Table 1. Eight samples were synthesized in a three-neck flask equipped with condenser, magnetic stirrer, thermocouple, heating mantle and an inlet of argon gas. In a typical process, a mixture of 2.0 g of $Fe(NO_3)_3{\cdot}9H_2O$, 10 mL of paraffin liquid, 10 mL of oleylamine (OLA) and 10 mL of oleic acid was heated to 150 °C for 60 min. Subsequently, the reaction mixture was heated up to 240 °C for 90 min, and then the temperature of the reaction mixture was decreased to 160 °C. At the same time, the $AgNO_3$ dissolved in OLA was injected into this reaction mixture. The mixture was kept at 160 °C for 30 min. After the reaction mixture were cooled down to room temperature, a mixture of hexane and ethanol was added to the solution, and the products could be separated from the suspension with a magnetic field. To remove the excess of the organic solvent and by-products completely, the products were washed several times with the mixture of hexane and ethanol by magnetic decantation, and then dried in a vacuum.

Table 1
The Ag/Fe molar ratios and Ag/Fe_3O_4 weight ratios in the samples.

Samples	atomic molar ratio Ag/Fe	weight ratio Ag/Fe_3O_4
1	0	0
2	0.06	0.025
3	0.12	0.05
4	0.18	0.075
5	0.24	0.1
6	0.30	0.125
7	0.36	0.15
8	0.48	0.2

2.2. Characterization

The powder diffraction data for Rietveld analysis were collected at room temperature with a Bruker D8 ADVANCE powder diffractometer (Cu-Kα radiation) and linear VANTEC detector. The step size of 2θ was 0.016°, and the counting time was 5 s per step. Rietveld refinement was performed by using TOPAS 4.2 [32].

The morphology, microstructure and local elemental composition of the NPs were investigated using transmission electron microscopy (TEM). TEM experiments were made with a JEM-2100 (JEOL Ltd.) microscope operating at the accelerating voltage of 200 kV. The microscope was equipped with an energy dispersive spectrometer (EDS), Oxford Instruments, what was used to control the elemental composition of the samples.

Magnetization field dependences at room temperature were measured with vibrating sample magnetometer (Lake Shore 7407). Temperature dependencies of magnetization were recorded with the quantum design SQID magnetometer for two cooling regimes – in the magnetic field of 500 Oe (FC) and without magnetic field (ZFC). The magnetization values are presented taking in to account the Fe_3O_4 content in samples according Table 1.

To carry out the MCD measurements, transparent composite plates containing the nanoparticles were prepared: the nanoparticles powder was mixed with dielectric transparent silicon-based glue (“Rayher” art. no. 3,338,100 80 mL) in the weight proportion 0.5/100 and measures were undertaken to obtain the homogeneous particles distribution in a matrix such as ultrasonic bath. The mixture was placed between two thin glass plates spaced by wires 0.15 mm in diameter and solidified. The low magnetic powder concentration allowed us to exclude the interaction between nanoparticles.

MCD was measured in the normal geometry: the magnetic vector and the light beam were directed normal to the samples plane. The modulation of the light wave polarization state from the right-hand to the left-hand circular polarization relatively to the magnetic field direction was used for the MCD measurements. The MCD value was measured as the difference between the optical density of samples for the right and left polarized light waves passing through them relatively to the magnetic field direction ($\Delta D = D_+ - D_-$) in the spectral range 1.2–3.5 eV in a magnetic field 13 kOe at the temperature 300 K. The measurement accuracy was about 10^{-4}, and the spectral resolution was 20–50 cm^{-1} depending on the wavelength.

3. Results and discussion

3.1. TEM analysis

TEM images are presented in Fig. 1 for three samples with different Ag/Fe_3O_4 ratios. For all samples, spherical or close to the spherical shape NPs are observed. The nanoparticle dimensions are very close for all samples. As it is seen from the log-normal distributions of the nanoparticles size for some samples, presented in the right panel in Fig. 1, the average particles size is 8 nm. Particles are collected in large conglomerates, as it will be shown below. Most of the particles are gray in color. There are also dark particles looking as if they are attached to the gray larger size particles. Similar pictures were observed by Tancredi with co-workers for the Ag/Fe_3O_4 heterocrystals prepared by a seed-assisted route in organic solvents of high boiling point (Figs. 2 and 3 in

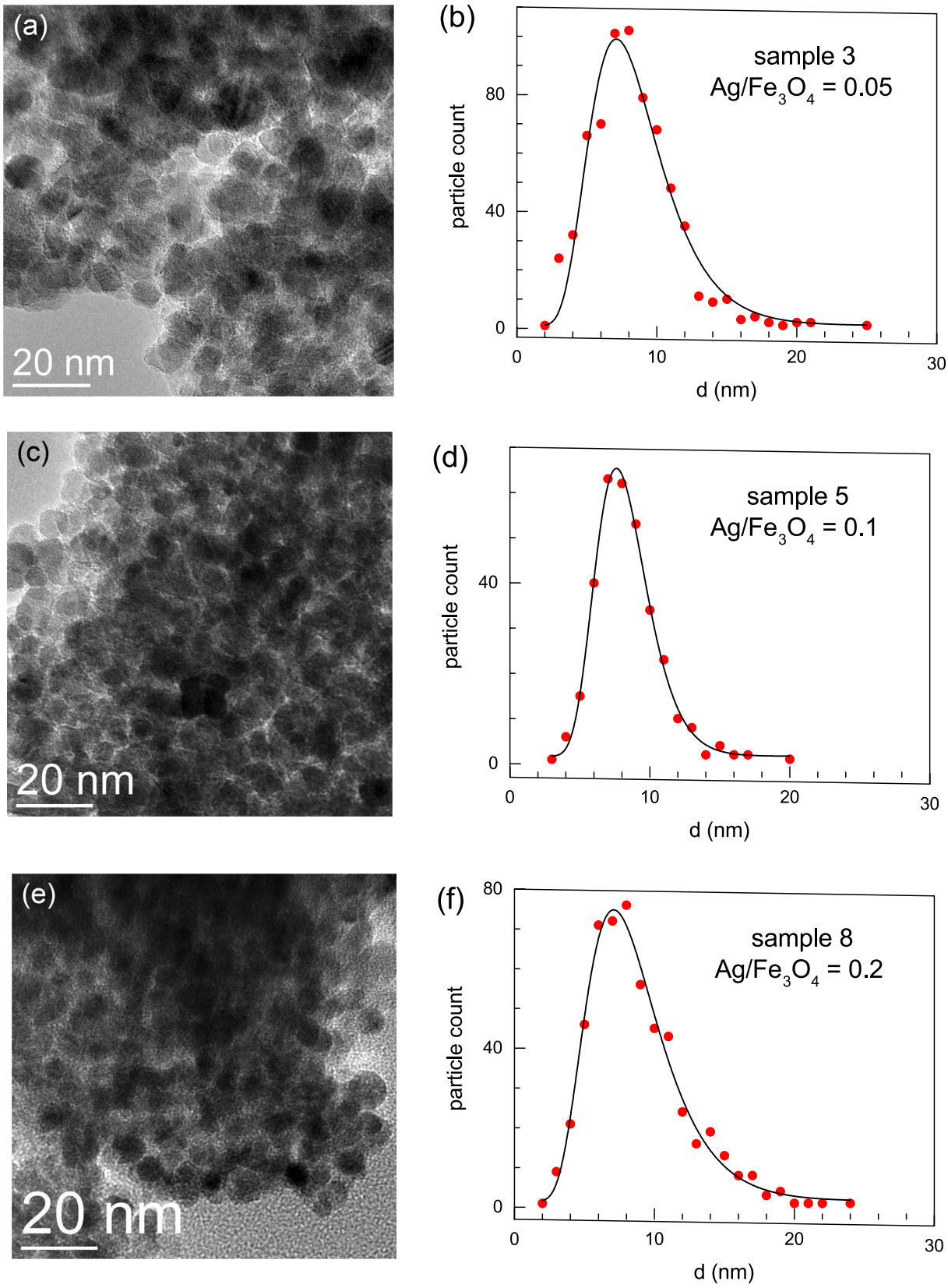

Fig. 1. TEM images of samples 3 (a), 5 (c), and 8 (e) and the log-normal average size distribution in samples 3 (b), 5 (d), and 8 (f).

[33]) and interpreted as dimers of Ag and Fe oxide. Appearance of such dimers was shown to effect significantly on the Fe oxide magnetic properties. Electron diffraction detected clearly the Fd–3 m crystal structure characteristic of magnetite Fe_3O_4 phase (ICDD PDF 4 + Card #04–005-4319). At the same time, no unambiguous reflections of the Ag crystal phase were observed. The reflex ≈2.37 Å can be attributed to fcc-Ag d(1 1 1) (Fm-3 m Ag (ICDD PDF 4 + Card # 00–004-0783)) the EDS data, but the Fe_3O_4 phase contains the reflex with the close

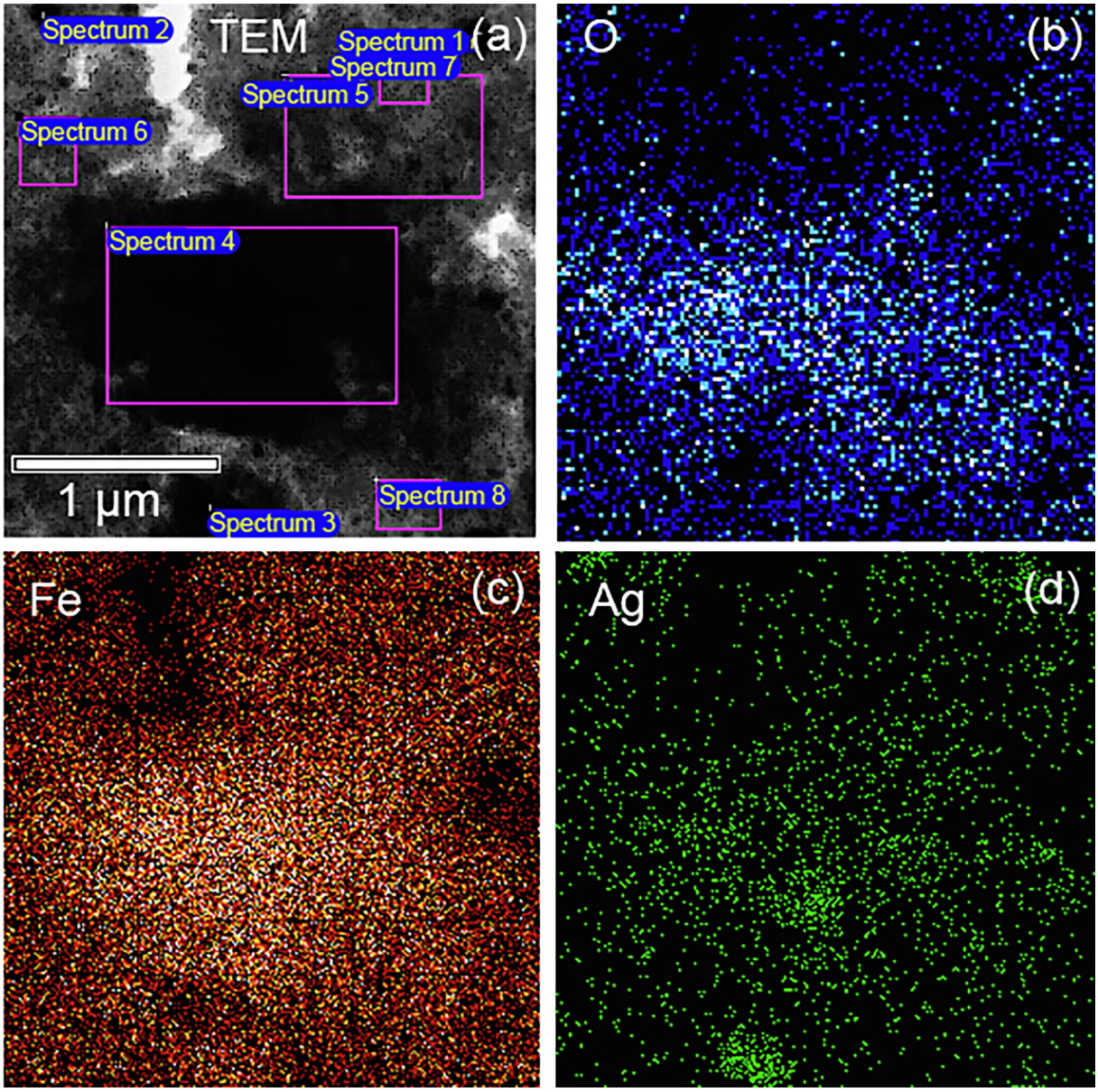

Fig. 2. STEM image of the NPs conglomerates (a), and corresponding EDS elemental mapping images of O (b), Fe (c) and Ag (d) of sample 3. Colored squares limit the areas for which the concentration of elements is indicated in the Table 2.

interplanar distance, true, it is of the weak intensity. At the same time reflexes fcc-Ag d(2 0 0) = 2.04 Å (I = 40%) and d(2 2 0) = 1.44 Å (I = 25%) absent in ED, possible because of low intensity.

Contrary to the particles morphology, the EDS elemental mapping images demonstrate different Ag distribution in the samples for the different Ag/Fe ratios as it is shown in Figs. 2–4 for samples 3, 5, and 8. It is seen that for all samples Fe and O are concentrated in the regions of the observed NPs. Ag presents also in these regions, but its presence also can be detected in areas containing no Fe and O. It is seen especially distinct for sample 5 (Fig. 3(c) and (d)), what corresponds to the large (~100 nm) dark particles in Fig. 3a. In sample 8 with the higher Ag concentration, this element is distributed uniformly over all NPs like Fe and O (compare Fig. 4(a) and (d)).

The element analysis results for some places designated in Fig. 2a and 3a by squares are presented in Tables 3 and 4, correspondingly. They confirm that the darker particles include more Ag, in comparison with gray particles. Two suppositions are possible on the Ag^{1+} ions localization in the areas occupied by particles. The Ag^{1+} ions can be distributed in the thin surface layer surrounding the magnetite NPs creating crystalline defects in them [34]. This layer should not be continuing by all means. Ag ions can diffuse also through the whole depth of the particle. In the last case the change of the lattice parameters should be observed because of the great difference between the Fe^{2+}, Fe^{3+}, and Ag^{+} ion radii – 0.078, 0.064, and 0.115 nm, correspondingly.

3.2. X-Ray analysis

Rietveld analysis was done for samples 5 and 8 differing from each other in the distribution of Ag. All peaks were indexed by two cubic phases with parameters close to Fe_3O_4 and Ag compounds. Therefore, these crystal structures were taken as starting model for Rietveld refinement. Refinement was stable and gave low *R*-factors (Table 4, Fig. 5). As it was mentioned above, if Ag^{+} ions entered the magnetite lattice, the lattice parameter would increase, since the ion radius of the silver is larger, but it turned out even slightly lower than the one indicated in the database (8.375–8.399 Å), so we can say with certainty that silver was not included in the magnetite lattice. It is seen also from

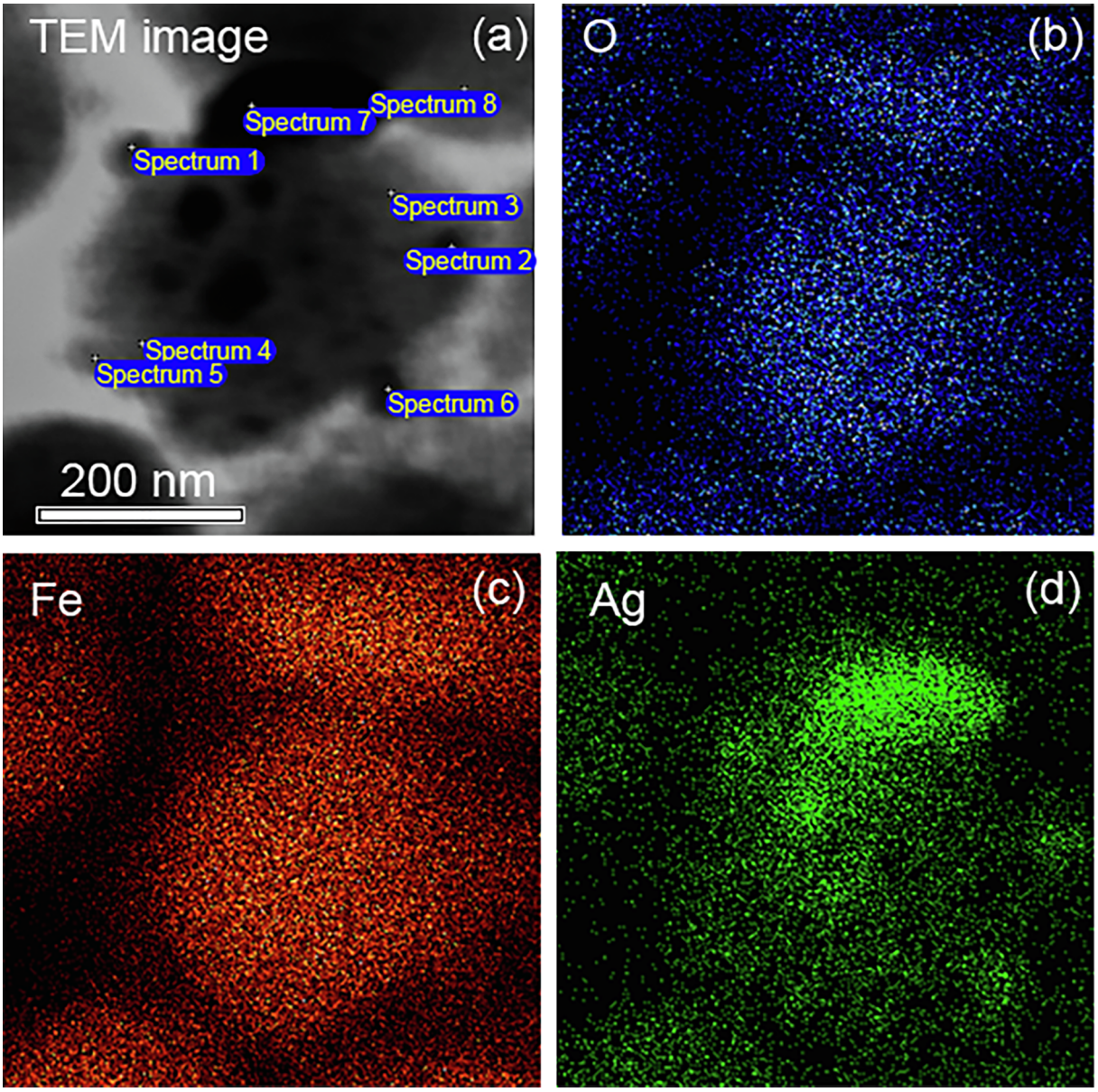

Fig. 3. STEM image of the NPs conglomerates (a), and corresponding EDS elemental mapping images of O (b), Fe (c) and Ag (d) of sample 5.

the XRD analysis that the components (Ag and Fe_3O_4) weight ratios correspond approximately to the weight ratio Ag/Fe_3O_4 from Table 1.

3.3. Magnetization

Magnetization dependencies on magnetic field for the samples investigated are shown in Fig. 6 (curve for sample 7 is not shown: it coincides totally with the curve for the sample 6). Shapes of these curves are the same for all samples and it is described by the Langevin curve that is characteristic for the superparamagnetic particles [35]. The tendency is seen to the M decrease with the Ag/Fe_3O_4 ratio increase. The M values in the saturated magnetic field (M_s) varies in the limits from 32 to 54 emu/g (comparing to the bulk Fe_3O_4 crystals 80 emu/g [36]) correspond to the other authors data for Fe_3O_4 nanoparticles fabricated with different techniques [10,26]. The M_s decrease with an increase of the Ag amount in these samples can be due to several reasons, including the Ag incorporation into nanoparticles, though this assumption is not consistent with the X-ray diffraction data.

Temperature dependences of the samples magnetization recorded in the field cooling (FC) and zero field cooling (ZFC) regimes are shown in Fig. 7 for samples 2 and 8. Similar thermomagnetic curves were observed for all other samples: FC and ZFC curves diverge at irreversibility temperature T_{irr}. At temperatures lower than T_{irr}, the ZFC curves pass below the FC curves and demonstrate a broad maximum centered at the blocking temperature T_b, after which magnetization decreases with temperature approaching to zero. These thermomagnetic curves indicate a superparamagnetic state of magnetite nanoparticles according to the Langevin shape of magnetization curves. As it is seen in the Inset in Fig. 7, T_{irr} and T_b shift (with small deviations) to lower temperatures with an increase of the Ag concentration in the samples. The simplest expression to estimate the blocking temperature looks as

$$T_b = Kv/25k_B, \quad (1)$$

where K is the anisotropy constant, v is the nanoparticle volume, k_B is the Boltzmann constant, the numerical coefficient is determined as $\ln(\tau_m/\tau_0)$, τ_0 is the relaxation time characteristic for the material, its typical value is between 10^{-9} and 10^{-10} seconds, τ_m is the measuring time. Usually $\ln(\tau_m/\tau_0)$ is of about 25. Considering the T_b decrease with the Ag concentration increase in the light of Eq.1, one can ascribe it to a decrease of the magnetite nanoparticles size [37], their anisotropy

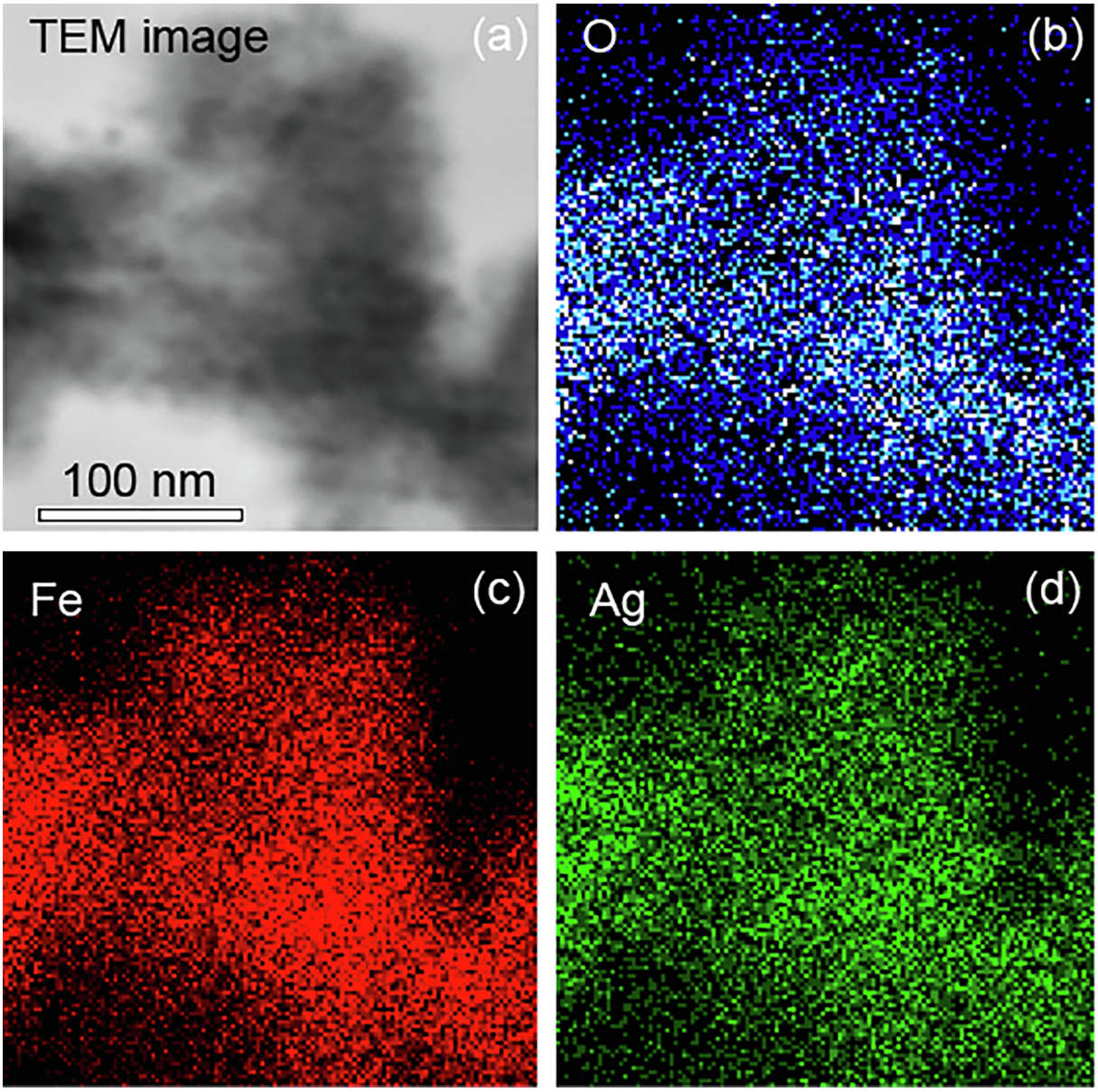

Fig. 4. STEM image of the NPs conglomerates (a), and corresponding EDS elemental mapping images of O (b), Fe (c) and Ag (d) of sample 8.

Table 2
Elemental analysis for different areas of sample 3 (Normalized).

Spectrum	O, atomic %	Cl, atomic %	Fe, atomic %	Ag, atomic %
Spectrum 1	26.90	1.42	37.60	34.08
Spectrum 2	35.39	1.21	36.81	26.58
Spectrum 3	25.22	0.56	41.73	32.50
Spectrum 4	43.50	1.05	51.43	4.02
Spectrum 5	26.38	1.49	68.12	4.02
Spectrum 6	32.73	1.62	61.66	3.98
Spectrum 7	21.38	1.63	72.73	4.26
Spectrum 8	45.55	1.17	50.55	2.73

Table 3
Element analysis for different areas of sample 5 (Normalized).

Spectrum	C, atomic %	O, atomic %	Fe, atomic %	Ag, atomic %
Spectrum 1	10.23	33.62	29.14	27.01
Spectrum 2	3.88	43.04	42.55	10.53
Spectrum 3	5.97	40.42	49.25	4.37
Spectrum 4	7.69	46.60	41.90	3.81
Spectrum 5	10.36	46.88	34.36	8.41
Spectrum 6	10.42	40.83	41.94	6.81
Spectrum 7	8.33	41.61	37.97	12.08
Spectrum 8	7.13	41.63	49.50	1.73

decrease [38], or change in the iron oxide phases [39] under an influence of the increasing Ag concentration. However, the nanoparticles average size is the same for all samples, as it is seen in Fig. 1(b, d, f), and, according to the X-ray patterns, only one phase presents in the powder samples. Therefore, the T_b and M_s decrease with the Ag concentration increase can be due to a decrease of the samples anisotropy. A change in magnetic behavior of the Ag/Fe_3O_4 nanostructure obtained by the silver seed assisted heterogeneous Fe_3O_4 nucleation was studied in Ref. [33]. However, opposite magnetization temperature behavior was observed in this reference: T_b in the Ag/Fe_3O_4 nanostructure was higher comparing to Fe_3O_4 nanoparticles. Perhaps this contradiction is due to different methods of synthesis of nanostructures used here (one step, in one pot) and in [40] (two steps). As a consequence, one can expect different character of interfaces between Fe_3O_4 and Ag

Table 4
Main parameters of processing and refinement of the samples 5 and 8.

Sample	Phase	Weight (%)	Space group	Cell parameters (Å), Cell volume (Å^3)	R_{wp}, R_p (%), χ^2	R_B (%)
5	Fe_3O_4	87(2)	*Fd*-3m	*a* = 8.363(2), *V* = 585.0(4)	0.89, 0.67,	0.16
	Ag	13(2)	*Fm*-3m	*a* = 4.088(1), *V* = 68.33(7)	1.36	0.31
8	Fe_3O_4	80(5)	*Fd*-3m	*a* = 8.368(7), *V* = 586(1)	1.26, 0.95,	0.20
	Ag	20(5)	*Fm*-3m	*a* = 4.090(4), *V* = 68.4(2)	1.32	0.51

nanoparticles in these two cases, that is, to incorporation of part of silver atoms into surface layers of the Fe_3O_4 nanoparticles. Such a mechanism could explain also the M_s decrease with an increase of the Ag concentration. On the other hand, a decrease of T_b with an increase of the Au or Ag shell thickness in structures Fe_3O_4/noble metal was observed in Ref. [41] and was associated with an influence of the dipole-dipole inter-particle interaction on their magnetic behavior.

3.4. MCD

MCD spectra of samples 1, 3, 5, 7, and 8 are shown in Fig. 8. For samples 2, 4, and 6 the spectra are close to that of sample 7. MCD spectrum of sample 1 containing no Ag is close to the magnetite MCD spectrum presented in literature for Fe_3O_4 thin film [23], for large NPs (~30 nm) [24], and for small NPs (3–8 nm) [25]. It is also close to the spectrum of the imaginary part of the off-diagonal component (ε''_{xy}) of the dielectric tensor, calculated from Kerr effect in bulk Fe_3O_4 crystal [42]. High energy and lower energy maxima of different signs are the predominant features of these spectra. However, the whole spectrum in our case is shifted to the lower energies comparing to MCD spectra in the cited references. Possible, the shift is due to the effect of silicon matrix. This problem requires additional investigation. As concerns the MCD sign, some authors use to choose the MCD sing arbitrarily. MCD sign in our case determined at the calibration procedure coincides with MCD sign in [23,24].

An increase in Ag concentration effects strongly in the MCD spectra shape of all samples. At that, the greater changes are observed for the lower energy (E < 2.2 eV) spectral region. In the high energy part of the spectrum, all samples demonstrate intense wide maximum centered at energies of 2.65–2.8 eV. The maximum shift to higher energies for some samples can be due to the overlapping of the MCD maximum of Fe_3O_4 and the surface plasmon resonance (SPR) in the Ag NPs. Indeed, SPR in Ag NPs was observed in the absorption spectrum near 2.8 eV [43].

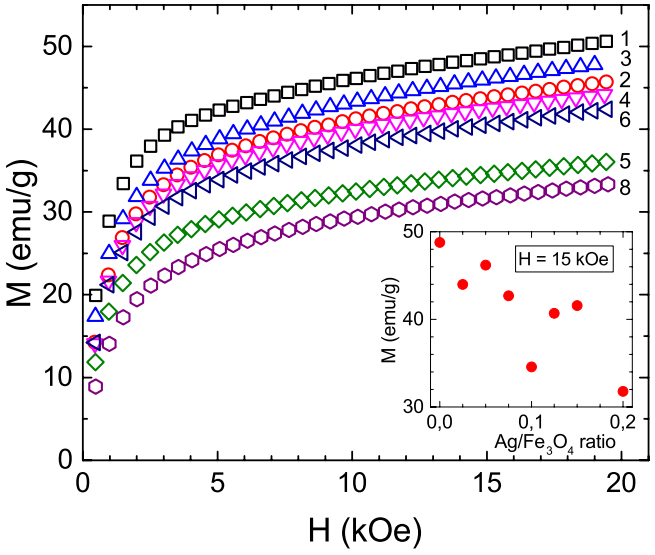

Fig. 6. Magnetization curves of all samples, except sample 7, recorded at room temperature. Magnetization curve of sample 7 coincides with that of sample 6. The magnetization values, M, were reduced to the Fe_3O_4 amount in each sample calculated according to Table 1. Insert: the magnetization value at H = 15 kOe in dependence on the weight ratio Ag/Fe_3O_4.

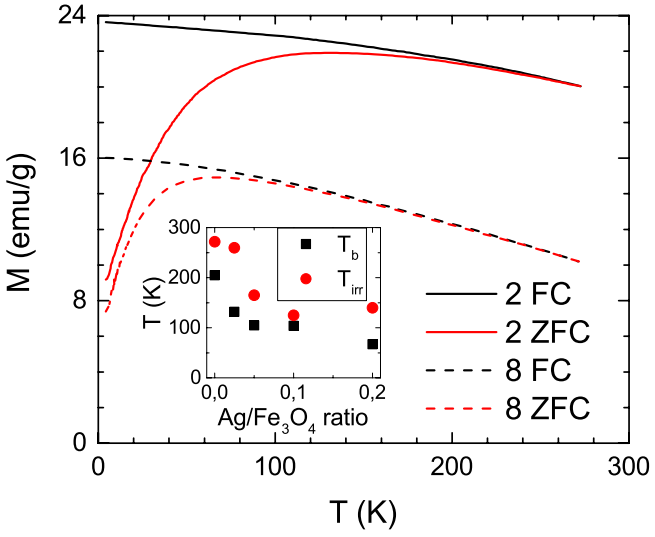

Fig. 7. FC and ZFC thermo-magnetic curves for samples 2 and 8 at H = 500 Oe. Insert: the dependencies of T_b and T_{irr} on the Ag/Fe_3O_4 ratio.

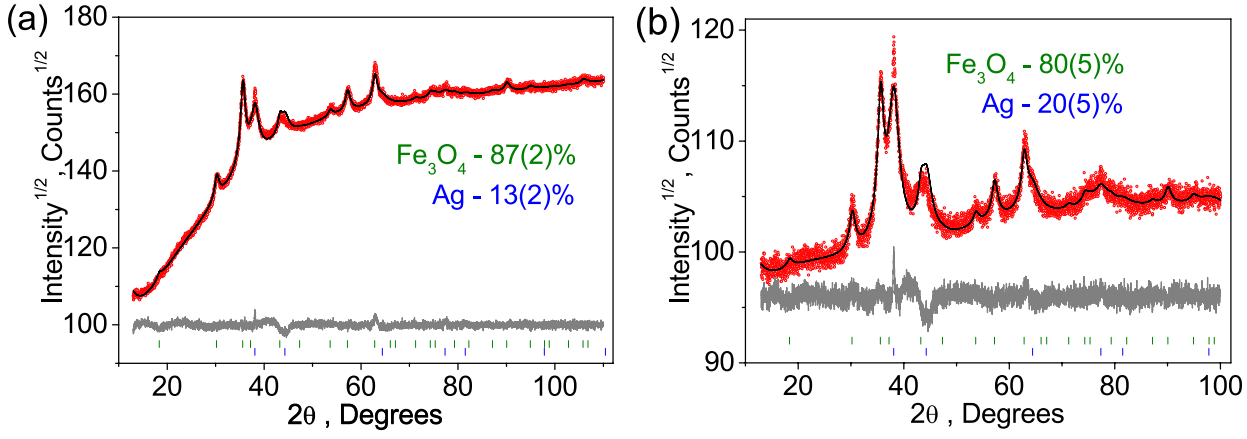

Fig. 5. Difference Rietveld plots of samples 5 (a) and 8 (b).

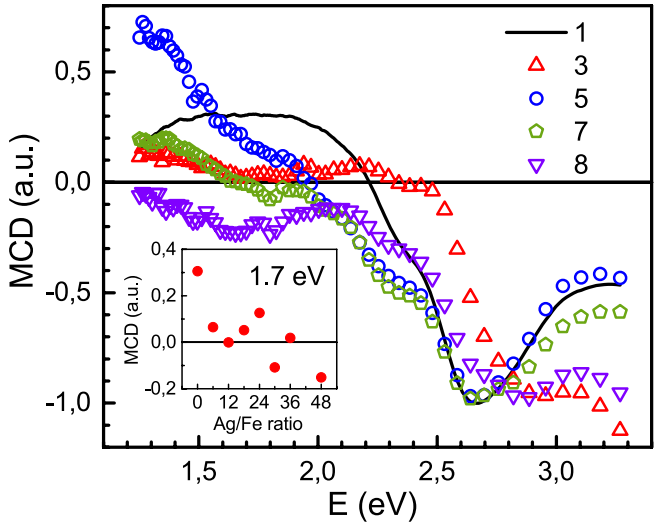

Fig. 8. Normalized magnetic circular dichroism spectra of several samples in dependence on Ag concentration at room temperature. H = 13 kOe. Amplitude of the high energy peak for each sample was taken as a unit. Insert: MCD normalized value of all samples at the light energy 1.7 eV.

Dramatic changes observed in the low energy part of the MCD spectrum (Fig. 8 insert) are caused, most probably, by the Ag effect in the probability of the electron transitions responsible for MCD in the specific spectral region. Note the great difficulties in the identification of the features in the Fe_3O_4 spectrum due to its complex cation composition: Fe^{3+} in octahedral (B) and tetrahedral (A) oxygen surroundings and Fe^{2+} in octahedral (B) positions. Authors of Refs. [26] and [44] associated the lower energy Fe_3O_4 positive MCD maximum observed for the Fe_3O_4 film near 2.2 eV (Fig. 9 in [26]) with the charge-transfer inter-band inter-valence transition $Fe_B^{2+}(a_{1g\uparrow}) \rightarrow Fe_B^{3+}(e_{g\uparrow})$, while the higher energy negative MCD peak near 3 eV (Fig. 9 in [26]) was ascribed to the inter-sublattice transition $Fe_B^{3+}(e_{g\downarrow}) \rightarrow Fe_A^{3+}(e_{\downarrow}t_{2\downarrow})$. Antonov et al. [44] considered also the inter-valence transition $Fe_B^{2+}(a_{1g\uparrow}) \rightarrow Fe_B^{3+}(t_{2g\uparrow})$ at about 0.9 eV. A larger set of electron transitions contributing to the MCD spectrum of Fe_3O_4 nanoparticles in the investigated spectral range was obtained in [27], when decomposing the experimental absorption and MCD spectra into equal quantities of Gaussian components. However the lower energy peak was associated with the $Fe_B^{2+}(a_{1g\uparrow}) \rightarrow Fe_B^{3+}(e_{g\uparrow})$ transition and one of the Gaussian components in the region of the higher energy peak was compared with the $Fe_B^{3+}(e_{g\downarrow}) \rightarrow Fe_A^{3+}(e_{\downarrow}t_{2\downarrow})$ transition analogously to [44]. At the same time, authors of [27] introduced Gaussian component centered at the point where experimental MCD passes through zero and associated it with the $Fe_B^{2+}(e_{g\downarrow}) \rightarrow Fe_A^{3+}(e_{\downarrow}t_{2\downarrow})$ contrary to Ref. [44] where this transition was referred to essentially lower energy. They also added several

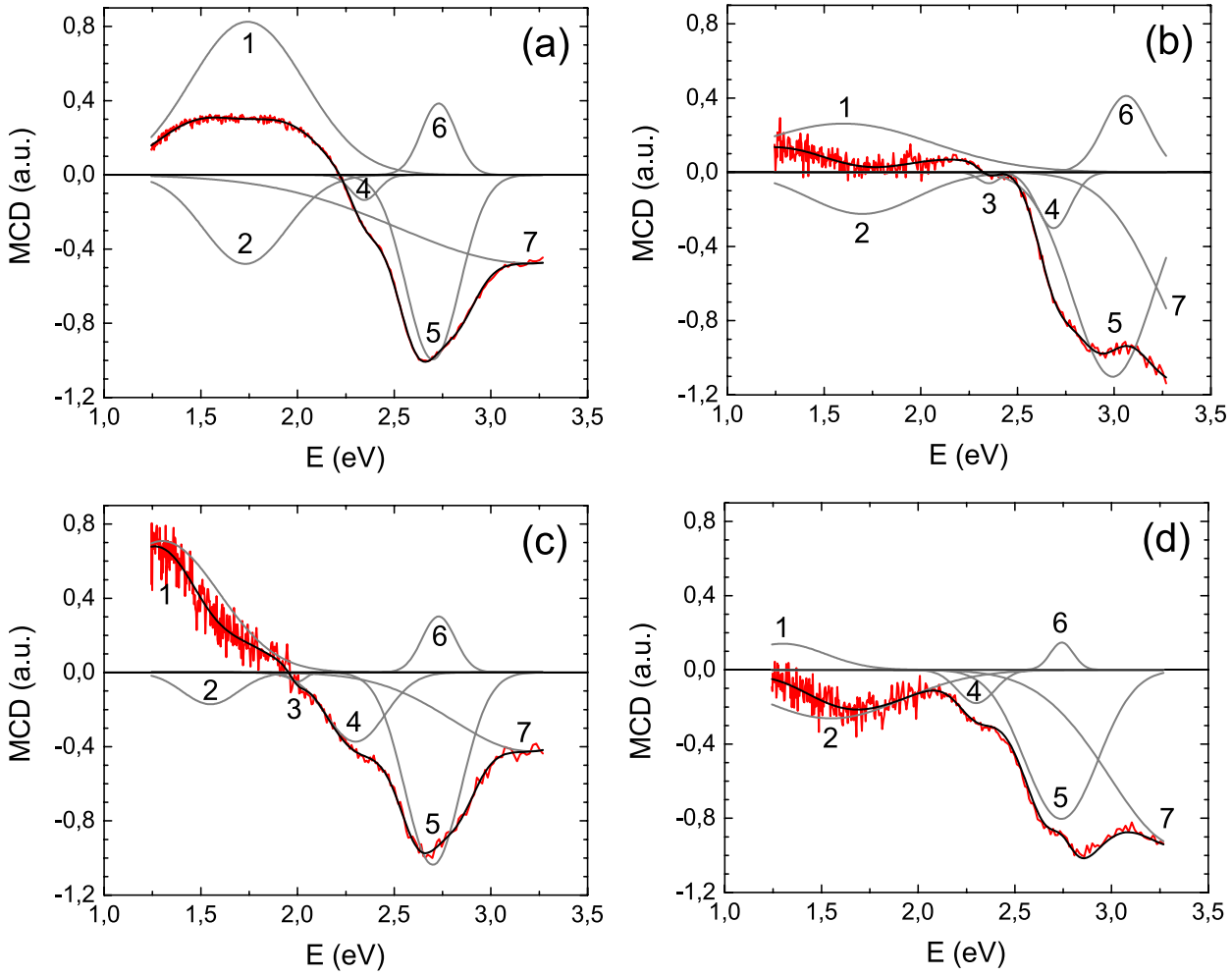

Fig. 9. The MCD spectra fitting by Gaussian peaks for samples 1, 3, 5, and 8, panels (a)-(d), respectively. Red lines indicate the experimental spectra; black curves are the sum of the Gaussian peaks (gray lines) indicated with numbers from 1 to 7.

peaks in the region of the higher MCD peak all associated with the $O2p \rightarrow Fe3d$ transitions. Nevertheless, both groups of authors considered lower and higher energy regions to be due to different kinds of transitions. Earlier, Kalska with co-authors [45] have made interpretation of the features in the Kerr effect spectrum of magnetite particles analogous to [44] interpretation. Quite recently J. Chen with co-authors [29] have carried out the first principal calculations to determine the main features of optical conductivity of cubic inverse spinel Fe_3O_4 and compared theoretical results with the MCD data on epitaxy-grown magnetite thin film single crystals. At that, they have taken into account more electron transitions comparing to [44,45]. In this connection, we have decomposed experimental MCD spectra for all samples into series of Gauss peaks so that the experimental curves are fitted by the minimum number of peaks. Best fitting was obtained taking into account seven peaks for all samples (Fig. 9). Peak energies appeared to be approximately the same for all samples, and were as follows: (1) 1.3, (2) 1.55, (3) 2, (4) 2.3, (5) 2.7, (6) 2.73, (7) 3.2 eV. Sample 3 was an exclusion from this series – the whole MCD spectrum of this sample was shifted by 0.3 eV to higher energies. Besides, peak (1) shifted to lower energies by 0.4 eV at the Ag addition. Comparing the peak energies with the electron transitions scheme presented in [29] we can refer the fitting peaks to the transitions: (1) $Fe_B^{2+}(t_{2g\downarrow}) \rightarrow Fe_B^{3+}(e_{g\downarrow})$, (2) $Fe_B^{2+}(e_{g\uparrow}) \rightarrow Fe_B^{3+}(t_{2g\uparrow})$, (3) $O(2p\downarrow) \rightarrow Fe_A^{3+}(e, t_{2\downarrow})$, (5) $Fe_B^{2+}(e_{g\uparrow}) \rightarrow Fe_A^{3+}(e, t_{2\uparrow})$, (7) $Fe_B^{2+}(e_{g\uparrow}) \rightarrow Fe_A^{3+}(e, t_{2\uparrow})$ and $Fe_A^{3+}(t_{2\uparrow}) \rightarrow Fe_A^{3+}(e, t_{2\uparrow})$. For peaks 4 and 6 there is no correspondence with [29], though the features in the MCD spectrum are seen in Fig. 7 in [29]. It could be weak contributions from the parity allowed one-ion d-d transition $^5T_{2g}$ (^5D) $\rightarrow$ ^5E_g (^5D) in Fe^{2+} ions or parity and spin forbidden one-ion d-d transition in Fe^{3+} ions. By the way, peak (3) can also be associated with such kind of transitions. It is seen from Fig. 9, that the stronger Ag effect on MCD is observed for the low energy part of the spectrum where the MCD features are due to the charge transfer transitions between iron ions, occupying octahedral positions.

Experiments carried out have shown that presence of Ag nanocrystals in the powdered samples and their close contacts with the Fe_3O_4 nanocrystals cause a decrease of the Fe_3O_4 saturation magnetization and the blocking temperature T_b approximately proportional to Ag concentration in a powder as well as the strong changes in the MCD spectrum. Considering changes in magnetization value and blocking temperature in the Ag/Fe_3O_4 structures obtained by a seed assisted heterogeneous nucleation process, authors of [33] have ascribed these changes to the interfacial effects at the boundaries between Fe_3O_4 NPs and noble metal NPs what can modify the superficial disorder, change the energy barriers and the magneto-crystalline anisotropy. Similar effects can play a major role in the modification of magnetic properties of the studied samples. As concerns MCD, this effect is due to the structure of the electron energy zones and to the probability of the charge transfers between them which also is affected by the structural and magnetic disorder. Size effect, probably, also can play role. Thought NPs mean sizes of different samples are close with each other, insignificant changes in size can lead to noticable changes in the interfacial area/volume ratio. It is seen well for samples 3 (8.2 nm) and 5 (~9 nm) (Fig. 1) when difference in size ~ 0.8 nm causes the change of the interfacial area/volume ratio of about 10%. Further study can elucidate this phenomenon more deeply.

4. Conclusion

The Ag modified magnetite NPs synthesized by the thermal decomposition of the of $Fe(NO_3)_3 \cdot 9H_2O$ and $AgNO_3$ mixture have been studied with X-ray diffraction, electron microscopy, magnetic measurements and optical magnetic circular dichroism in dependence on the Ag concentration in the mixture. X-ray diffraction patterns revealed two crystalline phases – magnetite nanocrystals and Ag nanocrystals. At that the ratio of these crystal phase amounts was equal to the weight ratio Ag/Fe_3O_4 when synthesizing samples. The Ag addition did not effect on the Fe_3O_4 lattice parameter, that was approximately equal to the parameter of bulk Fe_3O_4 for all Ag concentrations. NPs with size of 4–15 nm, which were agglomerated into large blocks, were observed in the electron microscope images. Elemental mapping detected Ag both near magnetite NPs (together with Fe and O) and as separate particles.

The Ag presence in the samples led to the magnetization decrease approximately linear in the Ag concentration with some deviations, the decrease of blocking temperature in the process of zero field cooled measurements, and strong changes in the low energy part of the MCD spectrum. MCD spectrum was decomposed into Gaussian components, which energies for samples containing only Fe_3O_4 NPs were compared with the electron transition energies obtained from the theoretical calculations for this compound. Ag presence in the samples did not change noticeably energies of the Gaussian components but effected strongly their intensities, especially in the lower energy spectral range.

Changes in the magnetic properties were associated with the interfacial effects. In the region of close contacts between two kinds of nanoparticles the interface can appear where Ag ions came into Fe_3O_4 lattice and replaced the Fe^{3+} ions in octahedral positions. Such an interface did not affect noticeably in the structural characteristics but causes significant changes in magnetic properties.

Acknowledgements

The reported study was funded by Russian Foundation for Basic Research, Government of Krasnoyarsk Territory, Krasnoyarsk Regional Fund of Science to the research project № 18-42-243021 and by Joint Research Project of Russian Foundation for Basic Research № 19-52-52002 and Ministry of Science and Technology, Taiwan MOST № 108-2923-M-153-001-MY3 and № 106-2112-M-153-001-MY3.

References

[1] E.J.W. Verwey, E.L. Heilmann, Physical properties and cation arrangement of oxides with spinel structures I. Cation arrangement in spinels, J. Chem. Phys. 15 (1947) 174–180, https://doi.org/10.1063/1.1746464.
[2] E.J.W. Verwey, P.W. Haayman, F.C. Romeijn, Physical Properties and Cation Arrangement of Oxides with Spinel Structures II. Electronic Conductivity, J. Chem. Phys. 15 (1947) 181–187, https://doi.org/10.1063/1.1746466.
[3] M. Salerno, J.R. Krenn, B. Lamprecht, G. Schider, H. Ditlbacher, N. Felidj, A. Leitner, F.R. Aussenegg, Plasmon polaritons in metal nanostructures: the opto-electronic route to nanotechnology, Opto-Electron. Rev. 10 (3) (2002) 217–224.
[4] M.P. Sharrock, R.E. Bodnar, Magnetic materials for recording: an overview with special emphasis on particles (invited), J. Appl. Phys. 57 (1985) 3919, https://doi.org/10.1063/1.334917.
[5] A. Jordan, R. Scholz, P. Wust, H. Schirra, T. Schiestel, H. Schmidt, R. Felix, Endocytosis of dextran and silan-coated magnetite nanoparticles and the effect of intracellular hyperthermia on human mammary carcinoma cells in vitro, J. Magn. Magn. Mater. 194 (1–3) (1999) 185–196, https://doi.org/10.1016/S0304-8853(98)00558-7.
[6] P. Gong, H. Li, X. He, K. Wang, J. Hu, W. Tan, S. Zhang, X. Yang, Preparation and antibacterial activity of Fe_3O_4@Ag nanoparticles, Nanotechnology 18 (28) (2007) 285604, , https://doi.org/10.1088/0957-4484/18/28/285604.
[7] B. Chudasama, A.K. Vala, N. Andhariya, R.V. Upadhyay, R.V. Mehta, Enhanced antibacterial activity of bifunctional Fe_3O_4-Ag core-shell nanostructures, Nano Res. 2 (12) (2009) 955–965, https://doi.org/10.1007/s12274-009-9098-4.
[8] A. Amarjargal, L.D. Tijing, I.T. Im, C.S. Kim, Simultaneous preparation of Ag/Fe_3O_4 core-shell nanocomposites with enhanced magnetic moment and strong antibacterial and catalytic properties, Chem. Eng. J. 226 (2013) 243–254, https://doi.org/10.1016/j.cej.2013.04.054.
[9] W.Q. Jiang, Y.F. Zhou, Y.L. Zhang, S.H. Xuan, X.L. Gong, Superparamagnetic Ag@Fe_3O_4 core-shell nanospheres: fabrication, characterization and application as reusable nanocatalysts, Dalton Trans. 41 (15) (2012) 4594–4601, https://doi.org/10.1039/C2DT12307J.
[10] R. Zhao, J. Xu, P. Tao, F. Shi, F. Yu, X. Zeng, C. Song, J. Wu, W. Shang, T. Deng, Clean water generation with switchable dispersion of multifunctional Fe_3O_4-reduced graphene oxide particles, Prog. Nat. Sci.: Mater. Int. 28 (4) (2018) 422–429, https://doi.org/10.1016/j.pnsc.2018.05.005.
[11] R. Moosavi, A. Afkhami, T. Madrakian, A simple cyanide sensing probe based on Ag/Fe_3O_4 nanoparticles, RSC Adv. 5 (21) (2015) 15886–15891, https://doi.org/10.1039/c4ra14806a.
[12] H.Y. Guo, A.W. Zhao, R.J. Wang, D.P. Wang, L.S. Wang, Q. Gao, H.H. Sun, L. Li, Q.Y. He, Generalized green synthesis of Fe_3O_4/Ag composites with excellent SERS activity and their application in fungicide detection, J. Nanopart. Res. 17 (12)

(2015) 494, https://doi.org/10.1007/s11051-015-3286-9.
[13] Y.F. Shan, Y. Yang, Y.Q. Cao, Z.R. Huang, Facile solvothermal synthesis of Ag/Fe_3O_4 nanocomposites and their SERS applications in online monitoring of pesticide contaminated water, RSC Adv. 5 (124) (2015) 102610–102618, https://doi.org/10.1039/C5RA17606A.
[14] C.Y. Jiang, X.Y. Ma, F. Yu, X.P. Shi, A.P. Yang, Y.P. Wang, Detection of Lead Ions with Fe_3O_4/Ag Core-Shell Nanoparticles, J. Nanosci. Nanotechnol. 16 (7) (2016) 7215–7219, https://doi.org/10.1166/jnn.2016.11345.
[15] Z.A. Elhouderi, D.P. Beesley, T.T. Nguyen, P. Lai, K. Sheehan, S. Trudel, E. Prenner, D.T. Cramb, M. Anikovskiy, Synthesis, characterization, and application of Fe_3O_4/Ag magnetic composites for mercury removal from water, Mater. Res. Express 3 (4) (2016) 045013, , https://doi.org/10.1088/2053-1591/3/4/045013.
[16] C.C. Qi, J.B. Zheng, Synthesis of Fe_3O_4—Ag nanocomposites and their application to enzymeless hydrogen peroxide detection, Chem. Pap. 70 (4) (2016) 404–411, https://doi.org/10.1515/chempap-2015-0224.
[17] J. Jiang, H.W. Gu, H.L. Shao, E. Devlin, G.C. Papaefthymiou, J.Y. Ying, Bifunctional Fe_3O_4–Ag Heterodimer Nanoparticles for Two-Photon Fluorescence Imaging and Magnetic Manipulation, Adv. Mater. 20 (23) (2008) 4403–4407, https://doi.org/10.1002/adma.200800498.
[18] C.P. Jiang, C.W. Leung, P.W.T. Pong, Self-assembled thin films of Fe_3O_4-Ag composite nanoparticles for spintronic applications, Appl. Surf. Sci. 419 (2017) 692–696, https://doi.org/10.1016/j.apsusc.2017.05.116.
[19] J. Du, C. Jing, Preparation of Thiol Modified Fe_3O_4@Ag Magnetic SERS Probe for PAHs Detection and Identification, J. Phys. Chem. C 115 (36) (2011) 17829–17835, https://doi.org/10.1021/jp203181c.
[20] W. Baaziz, B.P. Pichon, J.M. Greneche, S. Begin-Colin, Effect of reaction environment and in situ formation of the precursor on the composition and shape of iron oxide nanoparticles synthesized by the thermal decomposition method, CrystEngComm 20 (44) (2018) 7206–7220, https://doi.org/10.1039/c8ce00875b.
[21] S. Belaid, D. Stanicki, L.V. Elst, R.N. Muller, S. Laurent, Influence of experimental parameters on iron oxide nanoparticle properties synthesized by thermal decomposition: size and nuclear magnetic resonance studies, Nanotechnology 29 (2018) 165603, https://doi.org/10.1088/1361-6528/aaae59.
[22] J. Park, K. An, Y. Hwang, J.-G. Park, H.-J. Noh, J.-Y. Kim, J.-H. Park, N.-M. Hwang, T. Hyeon, Ultra-large-scale syntheses of monodisperse nanocrystals, Nat. Mater. 3 (2004) 891–895, https://doi.org/10.1038/nmat1251.
[23] K. Binnemans, D. Verboven, C. Görller-Walrand, J. Lucas, N. Duhamel-Henry, J.L. Adam, Optical absorption and magnetic circular dichroism spectra of neodymium doped fluorozirconate (ZBLAN) glass, J. Non-Cryst. Solids 204 (2) (1996) 178–187, https://doi.org/10.1016/S0022-3093(96)00406-1.
[24] W.R.A. Mason, Practical Guide To Magnetic Circular Dichroism Spectroscopy, Wiely-Interscience, John Wiley & Sons, NJ, 2007.
[25] J.R. Neal, A.J. Behan, A. Mokhtari, M.R. Ahmed, H.J. Blythe, A.M. Fox, G.A. Gehring, Magneto-optical study of the Verwey transition in magnetite, J. Magn. Magn. Mater. 310 (2) (2007) e246–e248, https://doi.org/10.1016/j.jmmm.2006.10.132.
[26] M.S. Alshammari, M.S. Alqahtani, H.B. Albargi, S.A. Alfihed, Y.A. Alshetwi, A.A. Alghihab, A.M. Alsamrah, N.M. Alshammari, M.A. Aldosari, A. Alyamani, A.M.H.R. Hakimi, S.M. Heald, H.J. Blythe, M.G. Blamire, A. Mark Fox, G.A. Gehring, H. Yao, Y. Ishikawa, Magnetic properties of In_2O_3 containing Fe_3O_4 nanoparticles, Phys. Rev. B 90 (2014) 144433, https://doi.org/10.1103/PhysRevB.90.144433.
[27] H. Yao, Y. Ishikawa, Finite Size Effect on Magneto-Optical Responses of Chemically Modified Fe_3O_4 Nanoparticles Studied by MCD Spectroscopy, J. Phys. Chem. C 119 (23) (2015) 13224–13230, https://doi.org/10.1021/acs.jpcc.5b03131.
[28] G.A. Gehring, M.S. Alshammari, D.S. Score, J.R. Neal, A. Mochtari, A.M. Fox, Magneto-optic studies of magnetic oxides, J. Magn. Magn. Mater. 324 (21) (2012) 3422–3426, https://doi.org/10.1016/j.jmmm.2012.02.057.
[29] J. Chen, H.-S. Hsu, Y.-H. Huang, D.-J. Huang, Spin-dependent optical charge transfer in magnetite from transmitting optical magnetic circular dichroism, Phys. Rev. B 98 (2018) 085141, https://doi.org/10.1103/PhysRevB.98.085141.
[30] Q. Chen, H. Wang, Q. Wang, Y. Pan, Plasmon enhanced faraday rotation in Fe_3O_4/Ag ferrofluids for magneto optical sensing applications, Plasmonics 13 (1) (2018) 353–363, https://doi.org/10.1007/s11468-017-0606-1.
[31] Q. Chen, Q. Wang, H. Wang, Q. Ma, Q. Chen, Surface plasmon resonance enhanced faraday rotation in Fe_3O_4/Ag nanoparticles doped diamagnetic glass, Plasmonics 13 (1) (2018) 163–174, https://doi.org/10.1007/s11468-016-0496-7.
[32] Bruker AXS TOPAS V4: General profile and structure analysis software for powder diffraction data. – User's Manual. Bruker AXS, Karlsruhe, Germany. 2008.
[33] P. Tancredi, O.M. Londono, P.C. Rivas Rojas, U. Wollf, L.M. Sokolovsky, M. Knobsl, D. Muraca, Strategies to tailor the architecture of dual Ag/Fe-oxide nano-heterocrystals – interfacial and morphology effects on the magnetic behavior, J. Phys. D Appl. Phys. 51 (29) (2018) 295303, , https://doi.org/10.1088/1361-6463/aaccc3.
[34] B. Aslibeiki, Nanostructural, magnetic and electrical properties of Ag doped Mn-ferrite nanoparticles, Curr. Appl Phys. 14 (12) (2014) 1659, https://doi.org/10.1016/j.cap.2014.09.025.
[35] X. Batlle, A. Labarta, Finite-size effects in fine particles: magnetic and transport properties, J. Phys. D: Appl. Phys. 35 (6) (2002) R15–R42, https://doi.org/10.1088/0022-3727/35/6/201.
[36] R. Pauthenet, Variation thermique de laimantation spontanee des ferrites de nickel, cobalt, fer et manganese, Comptes rendus 240 (1950) 1842.
[37] J.M. Orozco-Henao, D.F. Coral, D. Muraca, O. Moscoso-Londoño, P. Mendoza Zélis, M.B. Fernandez van Raap, S.K. Sharma, K.R. Pirota, M. Knobel, Effects of Nanostructure and Dipolar Interactions on Magnetohyperthermia in Iron Oxide Nanoparticles, J. Phys. Chem. C 120 (23) (2016) 12796–12809, https://doi.org/10.1021/acs.jpcc.6b00900.
[38] D. Muraca, A. Siervo, K.R. Pirota, From quenched to unquenched orbital magnetic moment on metallic@oxide nanoparticles: dc magnetic properties and electronic correlation, J. Nanopart. Res. 15 (2012) 1375, https://doi.org/10.1007/s11051-012-1375-6.
[39] P. Tancredi, P.C. Rivas Rojas, O. Moscoso-Londoño, U. Wolff, V. Neu, C. Damm, B. Rellinghaus, M. Knobel, L.M. Socolovsky, Synthesis process, size and composition effects of spherical Fe_3O_4 and FeO@Fe_3O_4 core/shell nanoparticles, New J. Chem. 41 (24) (2017) 15033–15041, https://doi.org/10.1039/C7NJ02558K.
[40] N.R. Jana, Y. Chen, X. Peng, Size- and Shape-Controlled Magnetic (Cr, Mn, Fe Co, Ni) Oxide Nanocrystals via a Simple and General Approach, Chem. Mater. 16 (20) (2004) 3931–3935, https://doi.org/10.1021/cm049221k.
[41] M. Mandal, S. Kundu, S.K. Ghosh, S. Panigrahi, T.K. Sau, S.M. Yusufc, T. Pal, Magnetite nanoparticles with tunable gold or silver shell, J. Colloid Interface Sci. 286 (1) (2005) 187–194, https://doi.org/10.1016/j.jcis.2005.01.013.
[42] X. Zhang, J. Schoenes, P. Wachter, Kerr-effect and dielectric tensor elements of magnetite (Fe_3O_4) between 0.5 and 4.3 eV, Solid State Commun. 39 (1981) 189–192, https://doi.org/10.1016/0038-1098(81)91076-0.
[43] H. Yao, T. Shiratsu, Nanoscale 8 (21) (2016) 11264–11274.
[44] V.N. Antonov, B.N. Harmon, V.P. Antropov, A.Ya. Perlov, A.N. Yaresko, Electronic structure and magneto-optical Kerr effect of Fe3O4 and Mg^{2+}- or Al^{3+}-substituted Fe_3O_4, Phys. Rev. B 64 (2001) 134410, https://doi.org/10.1103/PhysRevB.64.134410.
[45] B. Kalska, J.J. Paggel, P. Fumagalli, J. Rybczyński, D. Satula, M. Hilgendorff, M. Giersig, Magnetite particles studied by Mössbauer and magneto-optical Kerr effect, J. Appl. Phys. 95 (3) (2004) 1343–1350, https://doi.org/10.1063/1.1637134.